

View Article Online PAPER



Cite this: Phys. Chem. Chem. Phys., 2018, 20, 24453

The dimensional and hydrogenating effect on the electronic properties of ZnSe nanomaterials: a computational investigation†

Xiaodong Lv, Fengyu Li, * Jian Gong* and Zhongfang Chen * *

We performed a comprehensive first-principles study on the structural and electronic properties of ZnSe two-dimensional (2D) nanosheets and their derived one-dimensional (1D) nanoribbons (NRs) and nanotubes (NTs). Both hexagonal and tetragonal phases of ZnSe (h-ZnSe and t-ZnSe) were considered. The tetragonal phase is thermodynamically more favorable for 2D monolayers and 1D pristine ribbons, in contrast, the hexagonal phase is preferred for the edge-hydrogenated 1D NRs and NTs. The 2D h-ZnSe monolayer is a direct-bandgap semiconductor. Both the pristine zigzag nanoribbons (z-hNRs) and the corresponding edge-hydrogenated NRs gradual, convert from the direct-bandgap semiconducting phase into a metallic phase as the ribbon w au increases; the pristine armchair nanoribbons (a-hNRs) remain as semiconductors with indirect b incigors with increasing ribbon width, and edge hydrogenating switches the indirect-bandgap feature to the direct-bandgap character or the metallic character with different edge passivation styles. The 1D h-ZnSe single-walled nanotub as in both armchair and zigzag forms keep the direct-bandgap semice aucting property of the 2D court rport but with smaller band gaps. For the thermodynamically mree faro, able t-ZnSe monolayer, the int insic direct-bandgap semiconducting character is rather robust to derived 1D nanoribbons with edges unsaturated or hydrogenated fully, and 1D single-walled no totubes all preserve the direct bandgap semiconducting feature. Our systemic study provides der prinsights into the electronic properties of ZnSe-based nanomaterials and is helpful for experimentalists to design and fabricate ZnSe based nanoelectronics.

Received 15th July 2018, Accepted 3rd September 2018

DOI: 10.1039/c8cp04472d

rsc.li/pccp

1. Introduction

Since the discovery of graphene in 2004, great progress has been achieved in the field of two-dimensional (2D) materials. The 2D materials family has been continuously enrighed by new family members, such as transition-metal dichalonge adies (TMDCs), BN, silicene, germanane, GaS, phorphorene, 2D transition metal carbides and nitrides with the chemical formula $M_{n+1}X_n$ (M = Sc, Ti, V, Cr, Zr, Nb, Mo, H), Ta; X = C, N; n = 1-3), and various inorganic grapher, analogues (IGAs). 11 Generally, these 2D nanomaterials fective nigh specific surface areas, abundant active surfaces, light, high flexibility and transparency, 12 and have tunal le electronic, optical, catalytic, and electrochemical properties, which bring great promise for modern technology. 13-24 For example, single-layer MoS2, the

010021, China. E-ma 7. fengyuli@imu.edu.cn, ndgong@imu.edu.cn

^a Physical School of Sce. ce and Technology, Inner Mongolia University, Hohhot,

with a direct band gap (~ 1.8 eV) and relatively high on/off raw, which is regarded as a promising material for field effect cansistors.²⁵ Phosphorene, firstly isolated in the laboratory through mechanical exfoliation from bulk black phosphorus,²⁶ has a drain current modulation up to 10⁵ and carrier mobility up to 1000 cm² V⁻¹ s⁻¹, which makes it a potential candidate for future nanoelectronics applications.9

Among diverse 2D layered materials, group II-IV binary chalcogenides ZnX and CdX (X = S, Se, and Te) have attracted significant attention in recent years. 27-34,40 Due to the superior tunability in the electronic properties,31 semiconductors ZnX and CdX have long been of tremendous interest for a broad range of applications, including transistors, heterojunction diodes, photoconductors, and photovoltaic devices. 35-39 Recently, Sun et al. successfully synthesized a freestanding ZnSe monolayer with a four-atom thickness and quasi-honeycomb lattice by using a strategy involving a lamellar hybrid intermediate, and their photoelectrochemical tests demonstrated that this nanosheet has outstanding performance for solar water splitting. 40 This pioneering work inspired theoretical studies on the electronic structure and intrinsic properties of freestanding ZnSe monolayers, and various freestanding single-layer to multi-layer

most famous member of he TMDC family, is a semiconductor

^b Department of Chemistry, The Institute for Functional Nanomaterials, University of Puerto Rico, Rio Piedras Campus, San Juan, PR 00931, USA. E-mail: zhongfangchen@gmail.com

[†] Electronic supplementary information (ESI) available. See DOI: 10.1039/c8cp04472d

Paper

sheets of ZnX and CdX with or without honeycomb lattices have been proposed as synthesis targets. ^{28–33,41} Interestingly, a new structure of ZnSe monolayers with a tetragonal lattice (t-ZnSe)^{29,31} was predicted to be energetically more favorable than the experimentally synthesized pseudohexagonal ZnSe (ph-ZnSe) counterpart, ⁴⁰ and might have a superior incident photon-to-current conversation efficiency for solar water splitting. ^{29,31,32} Moreover, the electronic and optical properties of the doped

t-ZnSe monolayer, ^{41,42} its potential applications in photocatalysts and Li-ion batteries, ⁴³ and the photocatalytic properties of the tetragonal ZnS/ZnSe hetero-bilayer have also been theoretically investigated. ⁴⁴

Tunability of electronic properties of 2D materials is crucial for their applications in electronics and optoeletronics. Previous theoretical studies mainly focused on the structural properties and applications in photocatalysis and energy storage of 2D ZnSe sheets, but a few important issues related to ZnSe nanomaterials have not been addressed. For example, what are the stabilities of 1D ZnSe nanoribbons and nanotubes in hexagonal and tetragonal phases? How do the electronic characters of these 1D ZnSe nanomaterials vary compared to the 2D counterparts? In this article, we reported a systematic study of the stability of 1D ZnSe nanoribbons and single-walled ZnSe nanotubes, and compared their electronic properties to the 2D nanosheets. The computational results show that the dimensional effect is important to tune the electronic properties.

2. Computational methods

In this work, all the computations were performed with periodic density functional theory (DFT) with the plant wive basis set as implemented in the Vienna *ab initio*, imilation package (VASP). The ion-electron interaction as described with the projector augmented wave (PAW) method. The Perdew-Burke-Ernzerhof (PBE) functional under the generalized gradient approximation was used to describe the exchange and correlation. The plane-wave basis set with an energy cutoff of 500 V via

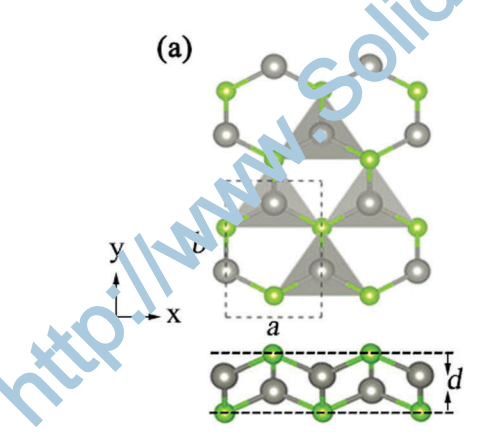
used through all computations. Brillouin zone sampling was adopted with Monkhorst–Pack (MP) special k-point meshes. The k grids for nanosheets, nanoribbons, and nanotubes were $10 \times 10 \times 1$, $1 \times 10 \times 1$ and $1 \times 1 \times 10$, respectively, for geometry optimizations. The vacuum space was larger than 10 Å between two adjacent images. Geometric structures were relaxed until the force on each atom is less than 1×10^{-4} eV Å $^{-1}$ and the energy convergence criteria is 1×10^{-5} eV Å $^{-1}$. For every system, the unit cell was optimized to obtain the lattice parameters corresponding to the lowest energy. Considering the underestimation of band gaps by the PBE functional, the Heyd–Scuseria–Ernzerh hybrid functional (HSE06) 51,52 was used to get more reliable band gap values.

To evaluate the stabilities of ZnSe monolayers, nanoribbons and nanotubes, we calculated the cohesive energy per atom (E_c) using the following definition: $E_c = (nE_{\rm Zn} + mE_{\rm Se} - E_{\rm ZnSe})/(m+n)$, where $E_{\rm Zn}$, $E_{\rm Se}$ and $E_{\rm ZnSe}$ represent the total energy of a Zn atom in bulk Zn, a Se atom in bulk Se, and the ZnSe per unit cell, respectively, and n(m) denotes the number of Zn (Se) atoms in a unit cell. According to this definition, systems with larger values (positive) of F_c are energetically more favorable. For the edge-hydrogenau a nunoribbons, the binding energy per H atom is defined is $E_c = (nE_{\rm H} + E_{\rm NR} - E_{\rm H-NR})/n$, where $E_{\rm H}$, $E_{\rm NR}/E_{\rm H-NR}$, and $E_{\rm NR}$ are the hilf energy of an isolated H₂ molecule, the total energy of profine/hydrogenated ZnSe NRs, and the number of H atoms, respectively. On the basis of this definition, systems with stronger binding strengths in we larger (positive) E_b .

3. Results and disscussion

3.1. The prostructive two-dimensional ZnSe nanosheets

We first third the 2D ZnSe monolayers in hexagonal and tetra to an phases (Fig. 1). The hexagonal structure (h-ZnSe) postesses Pmn21 symmetry (space group number 31), and the optimized lattice parameters are a = 3.97 Å and b = 5.85 Å. The orthogonal unit cell contains two Zn and two Se atoms; each Se (Zn) atom is surrounded by three Zn (Se) atoms. The nearest



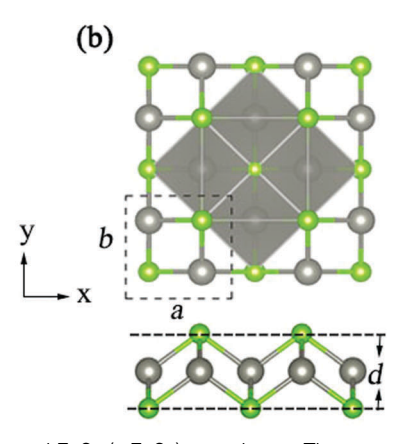


Fig. 1 Top and side views of (a) the hexagonal ZnSe (h-ZnSe) and (b) the tetragonal ZnSe (t-ZnSe) monolayers. The green and gray spheres represent Se and Zn atoms, respectively. The unit cells of h-ZnSe and t-ZnSe monolayers are highlighted by the dashed rectangle and square, respectively. a, b and d represent the lattice parameters of unit cells in the axial direction and the thickness of monolayer ZnSe, respectively.

Se–Se and Zn–Se distances are 3.97 Å and 2.39 Å, respectively, which are close to the experimentally measured values (4.01 Å and 2.46 Å, respectively). The hexagonal structure has four-atomic layers; each Zn atom is tricoordinated with three Se atoms, forming a buckled hexagonal network with a thickness (d) of 2.38 Å (Fig. 1a). The tetragonal phase (t-ZnSe) of ZnSe monolayers possesses P4/nmm symmetry (space group number 129), and the optimized lattice parameters are a = b = 4.10 Å. The tetragonal unit cell contains two Zn atoms and two Se atoms; each Zn (Se) atom is tetracoordinated with four Se (Zn) atoms. The t-ZnSe monolayer has three atomic layers, forming a buckled tetragonal network with a thickness (d) of 2.99 Å (Fig. 1b). Note that both the h-ZnSe and t-ZnSe monolayers are buckled instead of a planar structure, since the buckled surface can decrease the surface energy and then endow them with enhanced stability. 40,53

To compare their relative stabilities, we computed the cohesive energies of monolayer h-ZnSe and t-ZnSe. The cohesive energy of t-ZnSe (2.26 eV) is slightly larger than that of h-ZnSe (2.25 eV), which is in line with previous reports that the tetragonal structure is more stable. ^{29,31} The quite close cohesive energy of these two configurations of ZnSe monolayers stimulates us to estimate the relative proportions. Based on Boltzmann's distribution, as demonstrated by the Boltzmann factor (Fig. S1, ESI†), t-ZnSe dominates the monolayer structure at very low temperature, while when the temperature is higher than 50 K, both structures are in very similar probabilities.

Then, we studied the electronic properties of these two ZnSe monolayers. Since the PBE functional tends to underestimate the band gaps, we also used the HSE06 functional for band structure calculations. If not specified, the results in the following are from PBE computations.

As shown in Fig. 2(a), the h-ZnSe monolayer is a direct bandgap semiconductor. The PBE band gap is 2.34 eV, whereas the HSE06 value is about 3.40 eV, which is in good agreement with the experimental value (~ 3.50 eV).³¹ The partial charge density distribution corresponding to the valence-band maximum (VBM) and conduction-band minimum (CBM) (Fig. 2) indicates that both the VBM and CBM are contributed by Se atoms, and mainly from the Se p orbital. Because of the heteropolarity of the Zn-Se bonds, the electron-rich region is mainly near Se atoms. Similarly, the t-ZnSe monolayer also exhibits the semiconducting feature with a direct bandgap (2.11 and 3.30 eV, respectively, at PBE and HSE06 levels of theory). The VBM state is localized at the Se atoms and mainly composed of the Se p orbital. For the CBM, the state is localized at the Zn atoms and mainly composed of the Zn s orbital. To quantitatively estimate charge transfer between Zn atoms and Se atoms, Bader charge analysis⁵⁴. was performed. Our calculation results revealed that each Zr at m donates 0.69 and 0.70 e respectively to the neighboring Se atoms for the h-ZnSe and t-ZnSe monolayers; the computed electron transfer is in line with the larger electronegativity of Se (2.55) than Z (1.53).

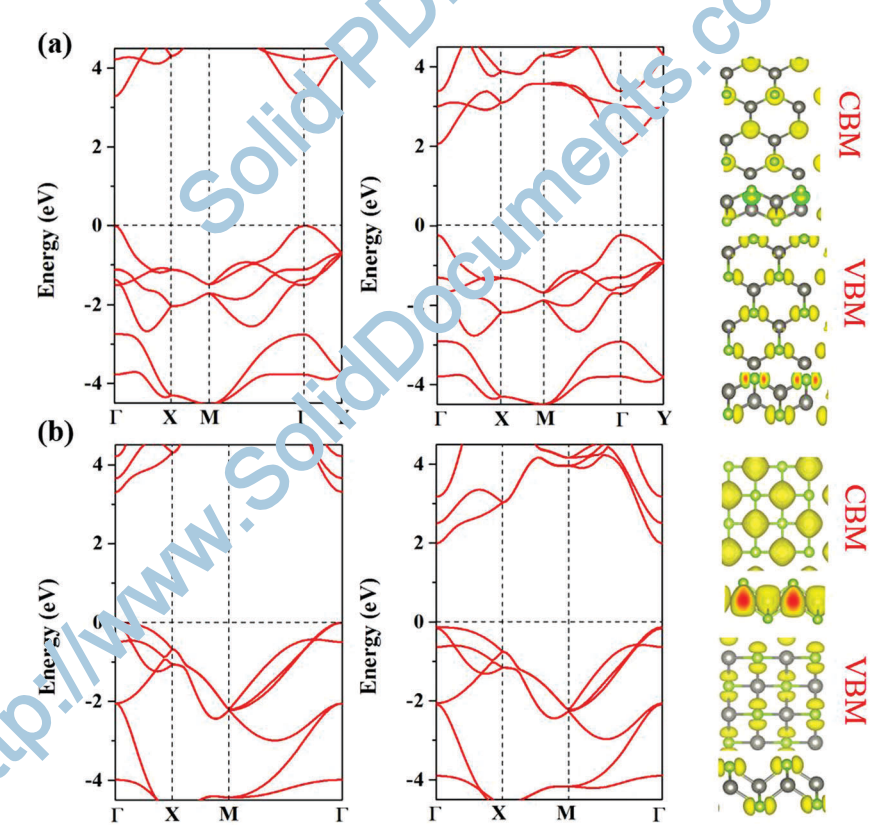


Fig. 2 HSE06 (left panel) and PBE (middle panel) band structures of the monolayers (a) h-ZnSe and (b) t-ZnSe. The Fermi level is set to zero as indicated by the horizontal dashed lines. The right panels in (a) and (b) show the partial charge density distributions of the valence band maximum (VBM) and the conduction band minimum (CBM). The isosurface value is 0.002 e Bohr⁻³. The green and gray spheres represent Se and Zn atoms, respectively.

Paper

3.2. The pristine one-dimensional ZnSe nanoribbons

On the basis of the above work, we continued to investigate the derived nanoribbons. It is expected that the ZnSe nanoribbons can display even more interesting electronic properties. In the present work, two types of ZnSe nanoribbons, namely armchair (a-hNRs) and zigzag (z-hNRs), can be obtained by cutting the hexagonal ZnSe monolayer along the *y*-axis and *x*-axis directions, respectively; however, only one type of ZnSe nanoribbons of the ZnSe tetragonal monolayer can be obtained (tNRs). Here we considered N = 4-17 (7.91–35.60 Å), 4-16 (11.69–46.77 Å) and 4-16 (8.21–32.82 Å) for a-hNRs, z-hNRs, and tNRs, respectively (*N* is the ribbon width). Fig. 3a–c show the structures of a-13-hNR, z-10-hNR and 10-tNR with a ribbon width of 13, 10 and 10, respectively.

Firstly, to examine the relative stabilities of these pristine ZnSe nanoribbons, we computed the cohesive energies for the a-hNRs, z-hNRs and tNRs *versus* the ribbon width N (see Fig. 4c). Systems with greater $E_{\rm c}$ values are energetically more favorable according to the definition in the Computational methods section. As discussed in Section 3.1, $E_{\rm c}$ of the t-ZnSe monolayer is slightly larger than that of 2D h-ZnSe. Expectantly, the cohesive energy of tNRs ($E_{\rm c}=2.14-2.22$ eV for N=4-15) is larger than those of z-hNRs ($E_{\rm c}=1.95-2.16$ eV for N=4-16) and a-hNRs ($E_{\rm c}=2.06-2.19$ eV for N=4-17) with the same ribbon width N, indicating that the tNRs are thermodynamically more favorable. For the hNRs, armchair nanoribbons are energetically preferr d

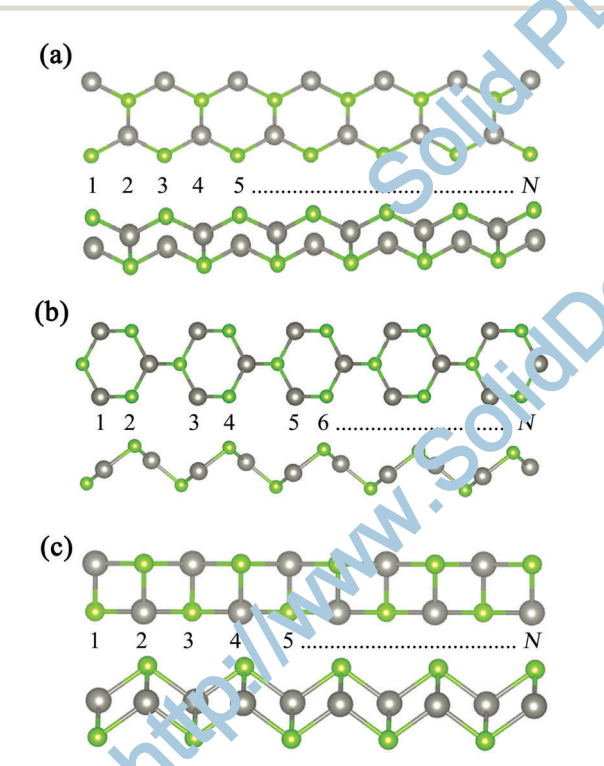


Fig. 3 Structures c´ZriSe nanoribbons with unpassivated edges (top and side views): (a) an armchair hexagonal ZnSe nanoribbon (a-hNRs), (b) a zigzag hexagonal ZnSe nanoribbon (z-hNRs) and (c) a tetragonal ZnSe nanoribbon (tNRs). *N* is the ribbon width. The green and gray spheres represent Se and Zn atoms, respectively.

since their $E_{\rm c}$ values are larger than zigzag ones of the same width N. The cohesive energy of the ZnSe nanoribbons increases gradually with increasing the ribbon width and gets close to $E_{\rm c}$ of the 2D counterparts (Fig. 4c). Experimentally, 2D h-ZnSe has been synthesized, ⁴⁰ and theoretically 2D t-ZnSe was predicted to be more stable than h-ZnSe, ³¹ thus it is very promising to achieve the 1D h-ZnSe and t-ZnSe nanoribbons.

Next, we studied the electronic structure and width-dependent characteristics of the ZnSe nanoribbons. The electronic band structures and the partial charge density corresponding to the VBM and CBM of a-7-hNR and 7-tNR are shown in Fig. 4a and b, which are representatives for the a-hNRs and tNRs, respectively. Our calculations revealed that the a-hNRs have an indirect bandgap character while the tNRs have a direct bandgap feature. Interestingly, with the increase of the ribbon width N, the electronic feature of z-hNRs can transfer from semiconductors with direct band gaps to metals when the ribbon width N reaches 7 (see Fig. S2, ESI†). For the a-hNRs, the VBM state is localized at the edges and is mainly composed of the Se p orbital; the CBM state distributes inside the ribbon and is also mainly composed of the Se p orbital, together with some contribution from the Zn. However, for the tNRs, the VBM is contributed by the p orbital of the ir ter or Se atoms, while the CBM is mainly contributed by the Zn atoms.

Furthermore, we investigated the variation of the band gap of a-hNRs, z-hNRs and tNRs at a function of nanoribbon width N (Fig. 4d). The band gap of the a-hNRs is larger than that of the tNRs at the same N (Fig. 4d), which resembles the wider band gap of the h-ZnSe monolyyer compared with the t-ZnSe monolayer. For the a-h was and tNRs, the band gap values generally decrease with local oscillations as the ribbon width N increases, and eventual, when N approaches infinity, the bandgap of the edge-uppess vated ZnSe NRs approaches that of monolayer ZnSe (2 34 eV and 2.11 eV for hexagonal and tetragonal phases, respectively, at the PBE level of theory). However, this expected convergence does not occur for the z-hNRs: when the ribbon width N reaches 7, z-hNRs become metallic. In order to explore the origin of the semiconductor-metal transition, we compared the structural characteristics and plotted the total density of states (TDOS) and local density of states (LDOS) of z-hNRs (see Fig. S2 and S3, ESI†). Our computed results revealed that the initial z-hNR structures with smaller ribbon width N, such as N = 4, 5, 6, are unstable and transform into analogous tNRs after structure optimizations and they have a direct bandgap character; the VBM states mainly originate from the p orbitals of the interior Se atoms and the CBM states are mainly contributed by the Zn s orbital. For the relatively larger ribbon width z-hNRs with $N \geq 7$, the structures retain the hexagonal feature, and the z-hNRs have metallic behaviors; we note that the metallic states across the Fermi level mainly originate from the Se p orbital and the Zn s orbital of inner atoms.

3.3. The edge-hydrogenated 1D ZnSe nanoribbons

The edge atoms with dangling bonds significantly influence the electronic properties of pristine nanoribbons; the passivation of edge atoms such as hydrogen may bring significant changes

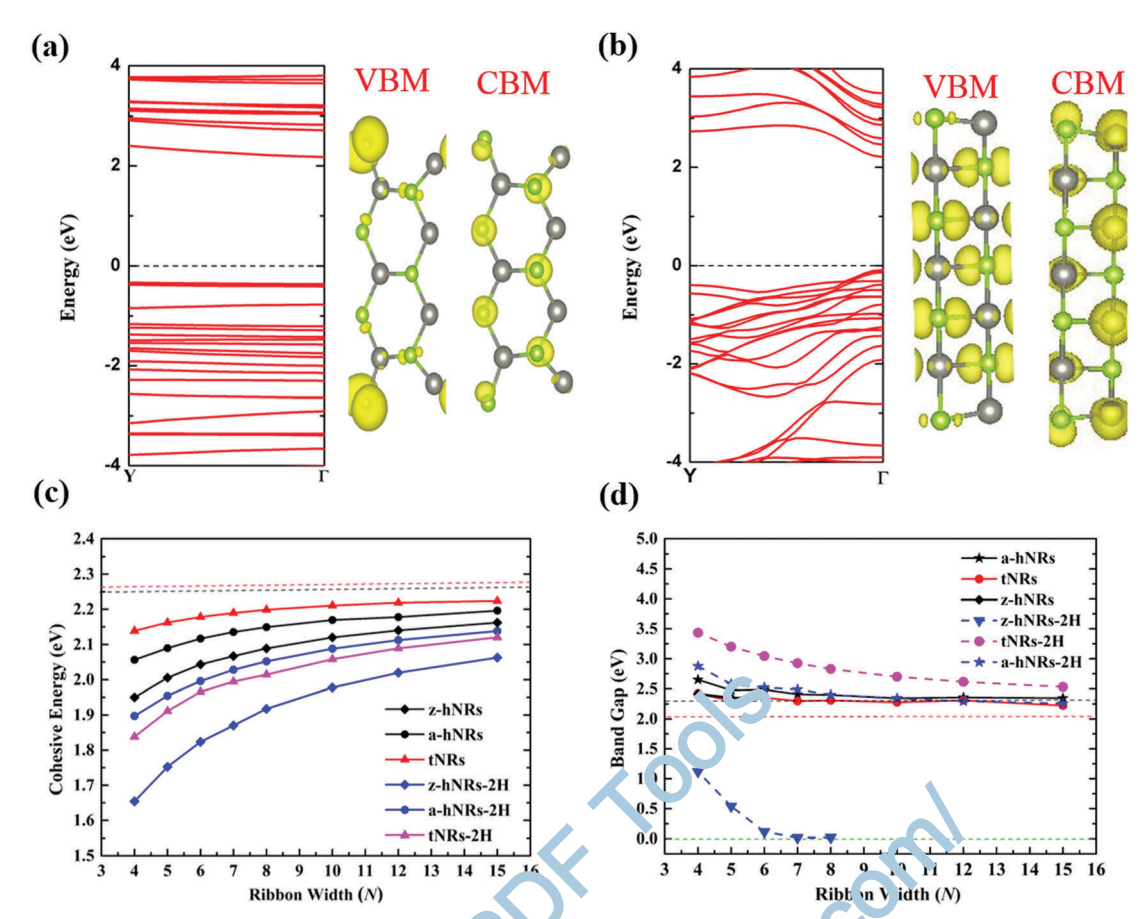


Fig. 4 The computed band structures of the pristine a-7-hNR a) and indicated by the horizontal dashed lines. The right panels in (a) and (b) display the partial charge density a tribution corresponding to the $V_{2}M$ and CBM. The isosurface value is 0.002 e Bohr⁻³. The green and gray spheres represent Se and Zn atoms, respectively. (c) The computed whest e energies per atom of both the pristine ZnSe nanoribbons and the edge-hydrogenated ZnSe nanoribbon, at both Zn and Se sites versus the nabon width N. (d) The computed bandgaps of the pristine ZnSe nanoribbons and edge-hydrogenated ZnSe nanor, be ns at both Zn and Se sites ver_{n-1} bbon width N ($4 \le N \le 16$). The black and red dash lines in (c) and (d) represent the bandgap of monolayer (nSt) in the tetragonal and the hexag ns. phase, respectively.

to the properties of the nanoribbons.^{56,57} Thus, besides the pristine ZnSe nanoribbons, i.e., the edge-unpassivated NRs, ve also investigated the structural and electronic properties of the edge-hydrogenated ZnSe nanoribbons (NRs-H). From vu. t.st calculations, we found that the average binding energy of a hydrogen atom for a-7-hNR saturated at the edge 2n site is 1.99 eV, which is ~ 0.43 eV lower than that of a-7. by λ saturated at the edge Se site (2.42 eV), indicating that the formation of Se-H bonds is more feasible than Zn-H bond formation. Previously, Tang et al. investigated the hydrogent on of Zn sites and O sites of ZnO nanosheets, and for a rtain thickness of ZnO sheets, Zn is more liable to form bonus with H.58 Providing that the hydrogen is excessive for 1 drogenating Se edge atoms, the formation of Zn-H bonds is highly possible. Thus, two situations of edge hy ro renation were considered: hydrogen saturation only . he Se edge sites (NR-1H), and edge hydrogenation with both edge Se and Zn atoms (NR-2H). Nanoribbons with the width N = 4-16, 4-15, and 4-15 were chosen for a-N-hNRs-nH, z-N-hNRs-nH and N-tNRs-nH as representatives to investigate the different configuration edge hydrogenation effects, respectively; *n* represents the number of

eds.-hydrogenated sites (n = 1 and 2 denotes hydrogenation only at the edge Se site, and both edge Se and Zn atoms, respectively). Fig. 5(a-f) represents the structures of a-15-hNR-nH, z-12-hNR-nH and 12-tNR-nH with a ribbon width of 15, 12 and 12, respectively. Clearly the edge atoms almost maintain the same configurations as in the 2D states.

In terms of the structural stability, the binding energies per hydrogen atom of the edge-hydrogenated hNRs at both the edge Zn and Se sites are 2.10, 2.11, 0.76 and 0.76 eV, respectively, for a-8-hNR-2H, a-10-hNR-2H, z-8-hNR-2H and z-10-hNR-2H; the corresponding values are both 1.85 eV for 8-tNR-2H and 10-tNR-2H (see Fig. S4, ESI†). Thus, edge-hydrogenated a-hNRs-2H are energetically more preferable than z-hNRs-2H and tNRs-2H.

In order to further evaluate the relative stability, we calculated the cohesive energy per atom (E_c) using the following definition: $E_c = (nE_H + mE_{Zn} + zE_{Se} - E_{H-ZnSe})/(n + m + z)$, where $E_{\rm H}$, $E_{\rm Zn}$ and $E_{\rm Se}$ are the half energy of an isolated H₂ molecule, and the total energy of a Zn atom in bulk Zn and a Se atom in bulk Se, respectively; $E_{\text{H-ZnSe}}$ is the total energy of hydrogenated ZnSe NRs, and n, m and z are the number of H, Zn and Se atoms in the ZnSe NR supercell, respectively. According to this definition,

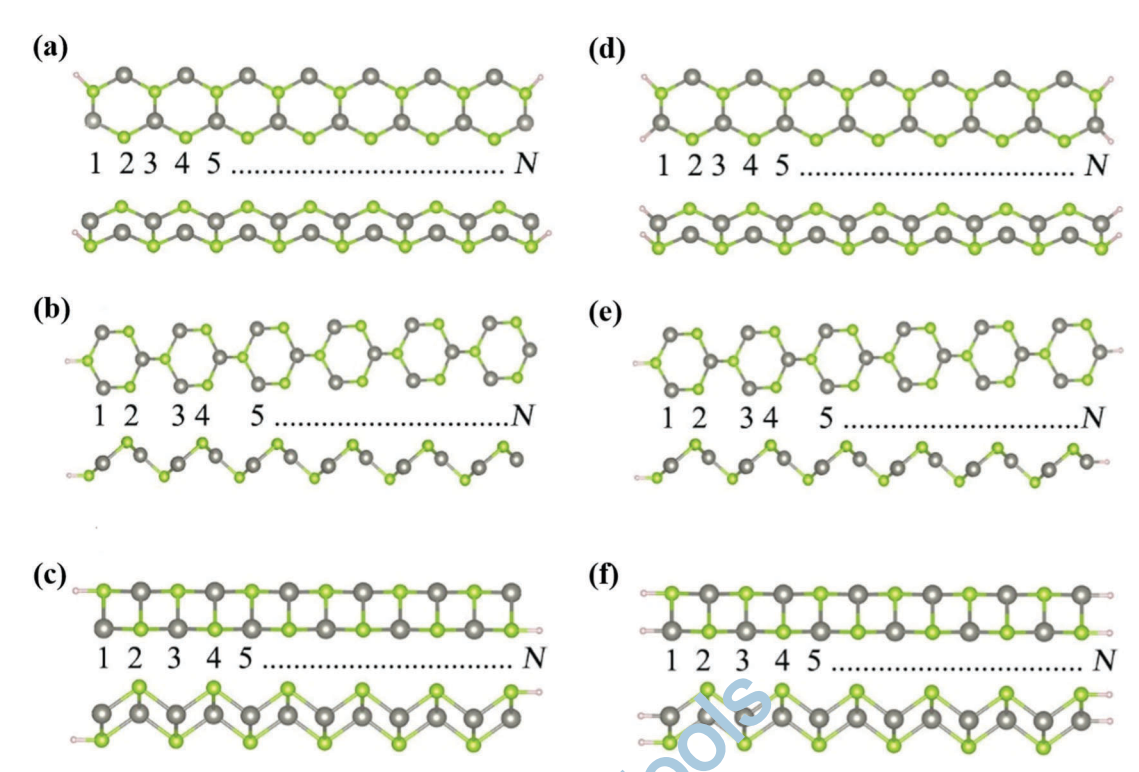


Fig. 5 Top and side views of (a) the armchair hexagonal ZnSe nanoribbon (a-1.5-l NR-1H), (b) the zigzag hexagonal ZnSe nanoribbon (z-12-hNR-1H), and (c) the tetragonal ZnSe nanoribbon with edge hydrogenation (12-tNR-1H), and (d) the armchair hexagonal ZnSe nanoribbon (a-15-hNR-2H), (e) the zigzag hexagonal ZnSe nanoribbon (z-12-hNR-2H) and (f) the tetragonal TnSe nanoribbon with edge hydrogenation (2-tNR-2H); N is the ribbon width. The green, gray and white spheres represent Se, Zn and H atoms, respectively.

systems with greater cohesive energy per atom are energetically more stable. For the edge-hydrogenated hNRs at only the edge Se sites, the cohesive energy of z-hNRs-1H ($E_c=1.56$ –1.17 eV for N=4–15) is larger than those of a-hNRs-1H ($E_c=1.90$ –2.14 eV for N=4–15) and tNRs-1H ($E_c=1.84$ –2.13 eV for N=4–15) with the same ribbon width N (see Fig. S5, Eart). Indicating that the z-hNRs-1H are thermodynamically more favorable. For the ZnSe NRs with hydrogenation at both edge Se and Zn sites, the cohesive energy of a-hNRs-2H ($E_c=1.89$ –2.13 eV for N=4–15) is larger than those of tNRs-2H ($E_c=1.83$ –2.12 eV for N=4–15) and z-h (Rs-2 H ($E_c=1.65$ –2.06 eV for N=4–15) with the same ribbon with N, that is, the a-hNRs-2H are also thermodynamically not a rable

(see Fig. 4c). These computed results are in line with the conclusion of previou. Line ng energy computations.

The passitation of Zn and Se atoms at the edges by hydrogen atoms sign fromtly affects the electronic properties. For the hydrogen passivated ZnSe nanoribbons only at the edge Se sites, we took the a-hNRs-1H, z-hNRs-1H and tNRs-1H with N=1 as the prototype to explore the electronic properties. The three ribbons all exhibit metallic character (see Fig. 6). We further investigated the variation of electronic properties of a-hNRs-1H, z-hNRs-1H and tNRs-1H with the nanoribbon width N (see Fig. S6–S8, ESI†); the Se-edge hydrogenated NRs are all metals independent of the ribbon width.

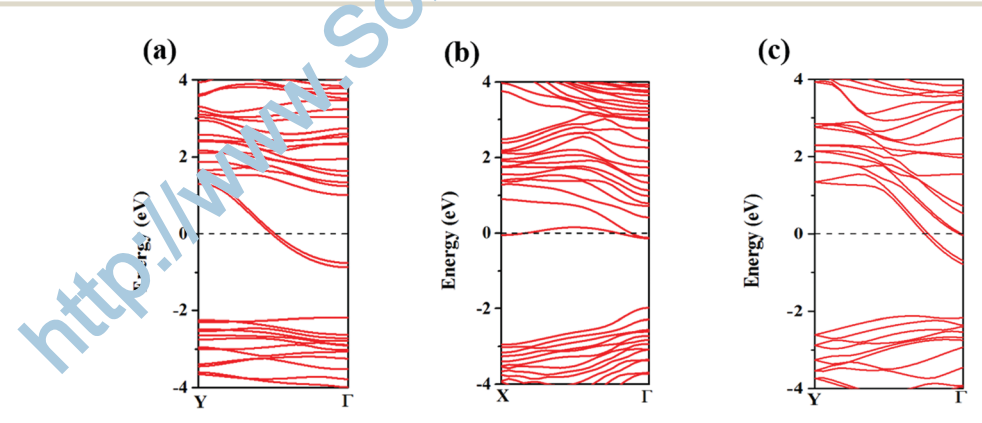


Fig. 6 The computed band structures (PBE) of (a) a-7-hNR-1H, (b) z-7-hNR-1H and (c) 7-tNR-1H. The Fermi level is set to zero as indicated by the horizontal dashed line.

Fig. 4d summarizes the variation of the band gap for the hydrogen saturated ZnSe nanoribbons at both the edge Zn and Se sites as a function of ribbon width N. For the z-hNRs-2H, their band structures follow the same trend as those of pristine nanoribbons: the direct bandgap of z-hNRs-2H decreases as the ribbon width increases, and the bandgap almost becomes zero (a metal) at N = 8 (Fig. 7a and b); the VBM and CBM are largely composed of the edge sides atoms. For the a-hNRs-2H, the indirect band-gap semiconductors are converted into direct band-gap semiconductors when the edge is passivated by hydrogen (Fig. 7c); the VBM is mainly composed of Se p orbitals while the CBM is distributed on the inner Se atoms. For tNRs-2H, the edge passivation by hydrogen preserves the direct-bandgap semiconducting property of the pristine ribbons; the VBM and CBM in tNRs are mainly contributed by the Se p orbitals and Zn s orbitals of the inner atoms, respectively (Fig. 7d), however, the bandgap values are markedly enlarged due to edge states (2.30 eV vs. 2.93 eV). For both a-hNRs-2H and tNRs-2H, the band gaps are large at small N, but approach those of the 2D counterparts as the width *N* increases, which can be easily understood by the quantum-size effect. At the same width, the band gap of a-hNR-2H is smaller than that of tNR-2H, which shows the opposite trend as the edgeunsaturated nanoribbons (see Fig. 4d). By comparing Fig. 7c and d and Fig. 4a and b, we could figure out that the edgehydrogenation alters the distributions of the VBM and CBM, and further alters the band gaps of the edge-hydrogenated NRs.

3.4. The one-dimensional single-walled ZnSe nanotube

A single-walled ZnSe nanotube can be viewed as rolling up 1 ZnSe nanosheet. Here three types of single-walled ZnS2 nanotubes,

namely, the armchair hexagonal ZnSe nanotubes (a-hNTs), the zigzag hexagonal ZnSe nanotubes (z-hNTs) and the tetragonal ZnSe nanotubes (tNTs), can be obtained by rolling up ZnSe monolayers. The configuration of any specific single-walled ZnSe-NT can be described with a pair of integer indexes (n_1, n_2) . Thus, there are three types of ZnSe nanotubes, namely z-hNTs, a-hNTs and tNTs, which are denoted as $(n_1, 0)$, (n_1, n_2) , and $(0, n_2)$, respectively. In this work, we investigated the structural and electronic properties of single-walled ZnSe-NTs with small diameters in the range of 10-19 Å, for which (6, 6), (10, 0) and (0, 10) nanotubes were chosen to represent armchair nanotubes, zigzag nanotubes in the hexagonal phase and nanotubes in the tetragonal phase, respectively (Fig. 8).

After structure optimization, we found there is no obvious structural parameter change for the a-hNTs, including the diameter (D) of the nanotube and the length of the unit cell (L_c) in the axial direction (Table 1). The optimized L_c of the a-hNTs decreases slightly as the diameter increases ($L_c = 3.97 \text{ Å}$ for D = 11.17 Å, and $L_c = 3.96$ Å for D = 18.61 Å). However, we found the z-hNT surface configuration undergoes reconstructions after geometry optimizations (see Fig. S9, ESI†); obviously, the tube well thacknesses of z-hNTs are thinner than those of pristine na lotubes, the atoms on the surface of the zigzag none ub) are arranged neatly to form a uniform plane and L_c gra qually increases with increasing D, from $L_c = 6.88 \text{ Å for } (8, 0)$ to $L_{\rm c}$ = 6.96 Å for (12, 0). Interestingly, for the tNTs with smaller diameters, such as (0, 8), (7, 9) and (0, 10), the initial tNT structures transform into a INTs after structure optimizations; the length of the univell (L_c) in the axial direction is also 3.97 Å, independent of the increase of the tube diameter.

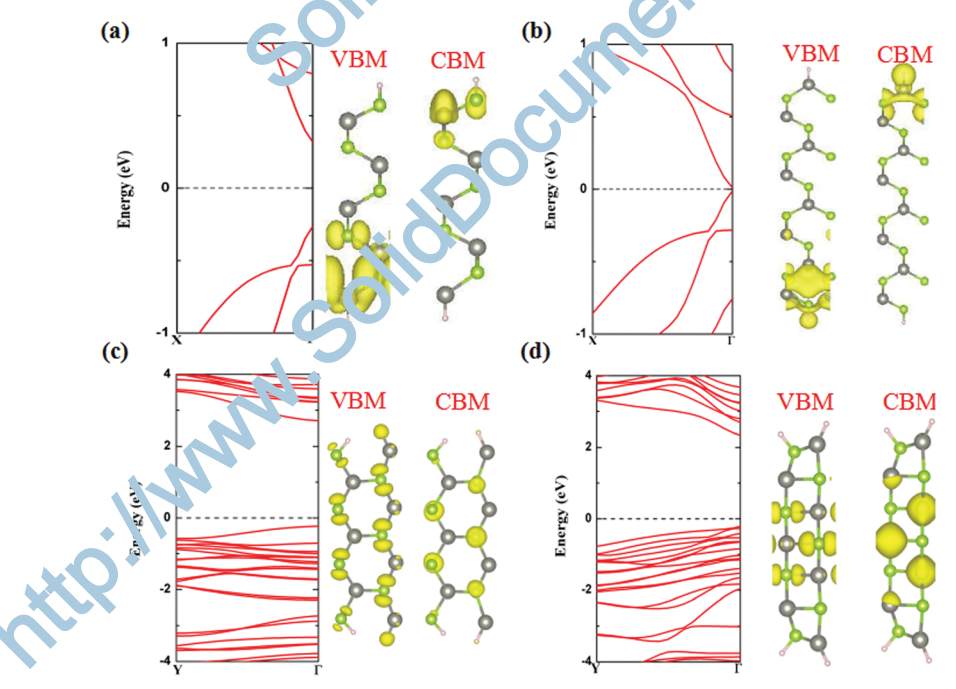


Fig. 7 The computed band structures (PBE) of (a) z-5-hNR-2H, (b) z-8-hNR-2H, (c) a-7-hNR-2H and (d) 7-tNR-2H. The corresponding partial charge density distributions of the VBM and CBM are displayed in the right panels. The isosurface value is 0.003 e Bohr⁻³. The Fermi level is set to zero as indicated by the horizontal dashed lines. The green and gray spheres represent Se and Zn atoms, respectively

Paper PCCP

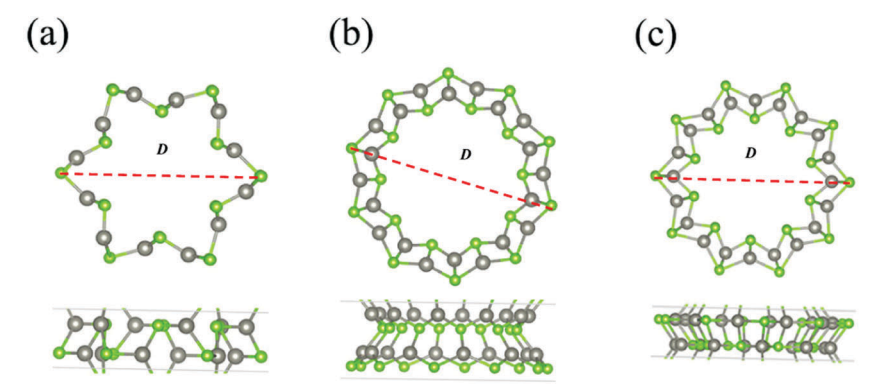


Fig. 8 Top and side views of the optimized (a) a-hNT (6, 6), (b) z-hNT (10, 0) and (c) tNT (0, 10). D is the diameter of the ZnSe nanotubes. The green and gray spheres represent Se and Zn atoms, respectively.

Table 1 The calculated diameters (*D*), length of the unit cell (L_c) in the axial direction, cohesive energy per atom (E_c), strain energy per atom (E_{str}), and bandgap (E_q) of ZnSe nanotubes (at the PBE level of theory)

Models	D (Å)	L_{c} (Å)	$E_{\rm c}$ (eV)	$E_{\rm str}$ (eV)	$E_{\rm g}$ (eV)
(6, 6)	11.17	3.97	2.78	0.02	2.29
(7, 7)	13.03	3.97	2.79	0.01	2.30
(8, 8)	14.89	3.97	2.79	0.01	2.30
(9, 9)	16.76	3.97	2.80	0.00	2.31
(10, 10)	18.61	3.96	2.80	0.00	2.31
(8, 0)	10.10	6.88	2.78	0.03	2.16
(9, 0)	11.13	6.90	2.77	0.03	2.12
(10, 0)	12.63	6.92	2.77	0.03	2.11
(11, 0)	13.87	6.94	2.77	0.03	2.08
(12, 0)	15.15	6.96	2.77	0.03	2 06
(0, 8)	10.45	3.97	2.79	0.02	2.3.
(0, 9)	13.06	3.97	2.79	0.02	2.31
(0, 10)	14.37	3.97	2.79	0.02	2.32
(0, 11)	15.68	4.13	2.70	0.11	1.12
(0, 12)	16.98	4.13	2.72	0.0	1.20

However, for tNTs with relatively larger diameters, such as (0, 11) and (0, 12), no obvious change in morphology was observed, and the tetragonal folded surface structure was maintained after structural relaxation; the length of the unit cell in the axial direction is almost independent of the diameter, showing the same trend as that of a-hNTs.

In order to evaluate relative stabilities of ZnSe paraubes, we calculated the cohesive energy per atom an strip energy per atom (E_{str}) . The strain energy per atom was defined as the difference of the cohesive energy per atom Letveen a perfect ZnSe monolayer and the ZnSe nanotube. The Estr values of a-hNTs, z-hNTs and tNTs with different tube cometers are presented in Table 1. Note that nanotubes with smaller strain energies per atom are energetically more favorable. As expected, the strain energy decreases with increasing D. Ve found that a-hNTs have lower E_{str} than that of z-hNTs and tNTs with similar diameters, implying the a-hNTs are more st. ble than z-hNTs and tNTs. For comparison, we also calculated the strain energies of the armchair (a-MoS₂-NTs) and zigzag (z-MoS₂ NTs) MoS₂ nanotubes (see Table S1, ESI†) with the similar diameters. The strain energies of ZnSe NTs are much smaller than those of the MoS₂ NTs. The in-plane stiffness of a 2D sheet is a key factor for the magnitude of the strain energy of the nanotubular derivatives. ⁶¹ We computed the in-plane stiffness of h-ZnSe and t-ZnSe, as well as the MoS₂ monolayer. The computed in-plane stiffnesses of the monolayer h-ZnSe (40.99 N m⁻¹) and t-ZnSe (40.81 N m⁻¹) are much smaller than that of the MoS₂ monolayer (129.55 N m⁻¹), suggesting the ZnSe monolayers are much less rigid than the MoS₂ monolayer, and as ϵ result, the ZnSe nanotubes have lower strain energies than MoS₂ nanotubes.

We rurther explored the electronic properties of the ZnSe nanotubes, for which the band structures of (10, 0), (6, 6), and (0, 10) and (0, 11) nanotubes were chosen as representatives for the z-hNTs, a-hNTs and tN Is, respectively (Fig. 9). All these types of nanotubes and irect-bandgap semiconductors; both the VBM and CB \sqrt{r} located at the Γ point, and are mainly contributed by Symoms (Fig. 9). The band gap values of these nanotubes and all smaller than their 2D counterparts (2.34 eV and 2.11 v or hexagonal and tetragonal phase, respectively). Rolling the hexagonal monolayer into armchair or zigzag nanotub's results in a slight decrease of band gaps, in contrast, a dramatic reduction of the band gap values occurs for the larger Lameter tetragonal phase (tNTs). For the armchair hNTs, the bandgap is almost independent of the diameter; the bandgap increases from 2.29 eV for D = 11.17 Å to 2.31 eV for D = 18.61 Å.For the zigzag hNTs, the bandgap decreases gradually from 2.16 eV for D = 10.10 Å to 2.06 eV for D = 15.15 Å. However, for the relative smaller (0, 8), (0, 9) and (0, 10) tNTs, because of the structural transition, the electronic structures are the same as a-hNTs, which keep the direct band-gap semiconducting feature, and the bandgaps are also independent of the diameter; while for the relatively larger diameter tNTs, the bandgaps are smaller than a-hNTs and z-hNTs, but the bandgap increases markedly with increasing the tube diameter (from $E_g = 1.12$ eV for $D = 15.68 \text{ Å to } E_g = 1.20 \text{ eV for } D = 16.98 \text{ Å}$).

4. Conclusion

In this work, we presented a detailed DFT study on the structural and electronic properties of 2D ZnSe nanosheets, and the derived 1D nanoribbons and nanotubes in both the h-phase and t-phase. Our computations show that the tetragonal

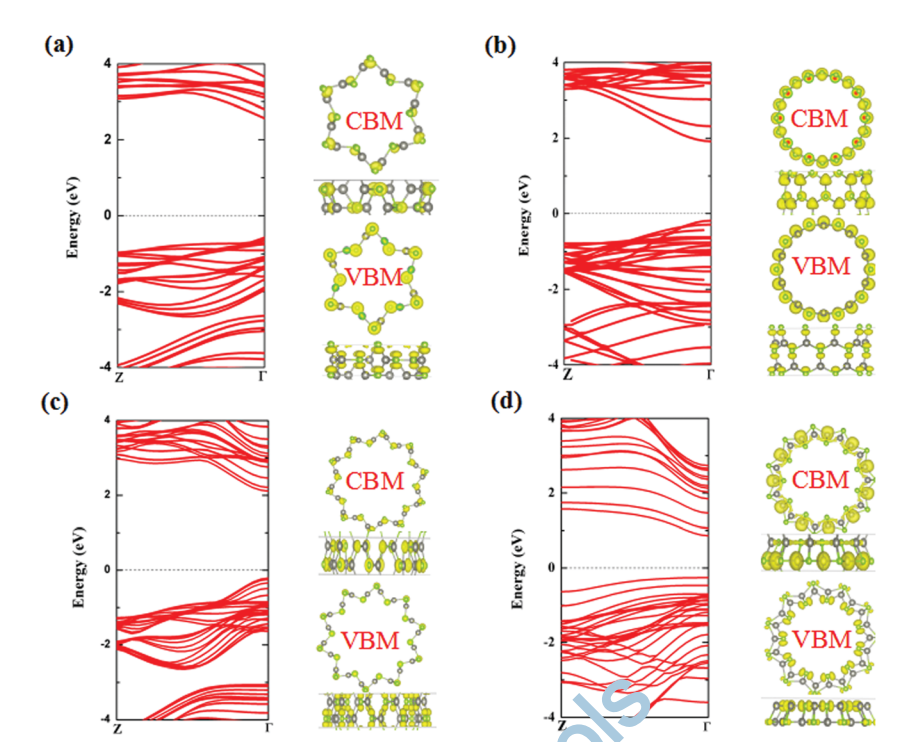


Fig. 9 Band structure (PBE) and the corresponding partial charge density distributions of the VBM (bottom panel) and CBM (up panel) of (a) armchair (6, 6) and (b) zigzag (10, 0) hNTs and (c) (0, 10) and (d) (0, 11) tNTs. The Fermi level is set to z to is indicated by the horizontal dashed lines. The isosurface value is 0.003 e Bohr⁻³. The green and gray spheres represent Se and Zn atoms, respectively.

monolayer is slightly more stable than the hexagonal counter part, and both monolayers are direct-bandgap semice advectors. Cutting the 2D nanosheets into 1D nanoribbons, the resulting NRs in the tetragonal phase (tNRs) also have higher stability compared to those in the hexagonal phase (hNr's). The tNRs are found to be direct band gap semicend ictors and the relatively more stable a-hNRs exhibitant indirect-bandgap semiconductor feature, while the less stable z-hNRs can be directbandgap semiconductors or metals depending on the ribbon width. When the edge is saturated by hydrogen atoms at the 7.1 and Se edge sites, the a-hNRs-2H become more stable than the tNRs-2H. The tNRs-2H are still direct-bandgap semiconducion the a-hNRs-2H restore the original direct-bandgap servicem actor character of the 2D counterpart. However, when any the edge Se sites are saturated by hydrogen atoms, the 2-hNPs 1H become more stable than the tNRs-1H; the a-hNRs-1H, -hNRs-1H and tNRs-1H all exhibit metallic character. When folding the 1D nanoribbons into 1D single-walled navituoes, the a-hNTs are also more stable than z-hNTs and n more stable than the tNTs; all these NTs are direct bangap semiconductors with smaller gap values than their 21) counterparts. For clarity, all the above findings are sumparized in Fig. 10.

The ZnSe monolaye say tetragonal and hexagonal phases are both kinetically stock demonstrated by all positive frequencies in the calcular of phonon spectra. Moreover, the Born-Oppenheimer more cular dynamics simulations of Li *et al.* revealed that at a fixed pressure of 700 MPa, the hexagonal ZnSe monolayer can be easily transformed to the tetragonal structure. We further investigated the thermodynamic stabilities of h-ZnSe

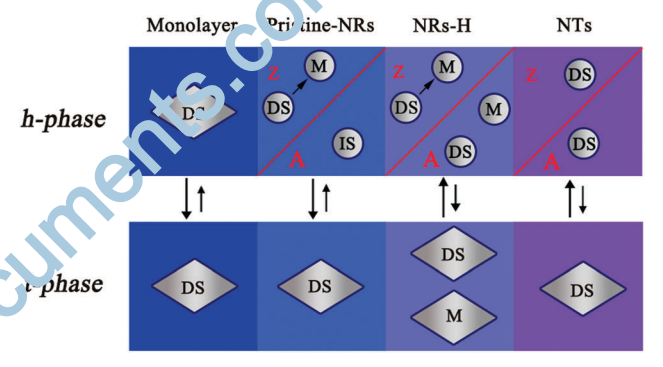


Fig. 10 The relative stabilities and electronic properties of the ZnSe monolayer, pristine nanoribbons, edge-hydrogenated nanoribbons (NRs-H), and nanotubes (NTs) in the h-phase and t-phase. DS, IS and M denote direct-bandgap semiconductors, indirect-bandgap semiconductors and metals, respectively. For the 1D derivatives, a larger Z/A means higher stability for zigzag/armchair nanoribbons/nanotubes.

and t-ZnSe *via* first-principles molecular dynamics (FPMD) simulations at 300 K. Both ph-ZnSe and t-ZnSe can well keep their original structures through 8 ps of FPMD simulation at 300 K, indicating the high stabilities of monolayer ZnSe, and after full atomic relaxation, the final h-ZnSe and t-ZnSe structures of FPMD simulations can easily recover their initial configurations (Fig. S10, ESI†). These results suggest that both h-ZnSe and t-ZnSe have good thermodynamic stabilities. Since the hexagonal ZnSe monolayer was successfully obtained by Xie's group [*Nat. Commun.*, 2012, 3, 1], 40 the tetragonal ZnSe monolayer is highly possible to be fabricated. By cutting and

rolling the 2D monolayer, 1D nanoribbons and single-walled nanotubes could be realized, respectively.

Our study provides deep understanding of the electronic properties of the ZnSe-based nanomaterials, and offers a simple and effective route to tune the electronic behavior of ZnSe nanostructures. Moreover, the recently synthesized 47 TMC compounds and heterostructures, 62 make us very optimistic to experimentally achieve those ZnSe-based nanomaterials.

Conflicts of interest

Paper

There are no conflicts to declare.

Acknowledgements

This work was supported in China by the National Nature Science Foundation of China (No. 11464032) and Startup Project of Inner Mongolia University, and in USA by NSF-CREST Center for Innovation, Research and Education in Environmental Nanotechnology (CIRE2N) (Grant Number HRD-1736093).

References

- 1 A. K. Geim and K. S. Novoselov, The rise of graphene, *Not. Mater.*, 2007, **6**(3), 183–192.
- 2 Q. Tang and Z. Zhou, Graphene-analogous low-dimentional materials, *Prog. Mater. Sci.*, 2013, **58**(8), 1244–131 v.
- 3 Q. Tang, Z. Zhou and Z. F. Chen, Innovation and discovery of graphene-likematerials via density-function at the corporations, *Comput. Mol. BioSci.*, 2015, 5(5), 363–379.
- 4 S. Manzeli, D. Ovchinnikov, D. Pasquie, C. V. Yazyev and A. Kis, 2D transition metal dich. 2 co enides, *Nat. Rev. Mater.*, 2017, 2(8), 1–15.
- 5 K. Watanabe, T. Taniguchi and H. Kanda, Direct-bandgap properties and evidence for ultraviolet lasing of hexagon a boron nitride single crystal, *Nat. Mater.*, 2004, 3(6), 404-409.
- 6 P. Vogt, P. De. Padova, C. Quaresima, J. Avila, E. Frant es. al. s, M. C. Asensio, A. Resta, B. Ealet and G. Le Ley, Sil cene: compelling experimental evidence for graphone like two-dimensional silicon, *Phys. Rev. Lett.*, 2012 108,15, 155501.
- 7 E. Bianco, S. Butler, S. Jiang, O. D. Restrepo W. Windl and J. E. Goldberger, Stability and exfolia ior of germanane: a germanium graphene analogue, 1.75 Nano, 2013, 7(5), 4414–4421.
- 8 D. J. Late, B. Liu, H. S. S. P. Matte, C. N. R. Rao and V. P. Dravid, Rapid characterization of ultrathin layers of chalcogenides on SiO₂/3i substrates, *Adv. Funct. Mater.*, 2012, 22(9), 1894–190.
- 9 L. Li, Y. Yu, T. J. e, Q. Ge, X. Ou, H. Wu, D. Feng, X. H. Chen and Y. Zhang, Black phosphorus field-effect transistors, Nat. Nanotechnol., 2014, 9(5), 372–376.
- 10 M. Naguib, V. N. Mochalin, M. W. Barsoum and Y. Gogotsi, MXene: a new family of two-dimensional materials, *Adv. Mater.*, 2014, 26(7), 992–1005.

- 11 C. N. R. Rao, H. S. S. Ramakrishna Matte and U. Maitra, Graphene analogues of inorganic layered materials, *Angew. Chem., Int. Ed.*, 2013, 52(50), 13162–13185.
- 12 H. W. Zhu and M. Wang, Two-dimensional materials: structure, preparation and properties, *J. Chin. Ceram. Soc.*, 2017, 45(8), 1043–1053.
- 13 A. Kara, H. Enriquez, A. P. Seitsonen, L. C. Lew Yan Voon, S. Vizzini, B. Aufray and H. Oughaddou, A review on silicenenew candidate for electronics, *Surf. Sci. Rep.*, 2012, **67**(1), 1–18.
- 14 A. J. Mannix, B. Kiraly, M. C. Hersam and N. P. Guisinger, Synthesis and chemistry of elemental 2D materials, *Nat. Rev. Chem.*, 2017, 1, 1–14.
- 15 C. L. Tang and H. Zhang, Two-dimensional transition metal dichalcogenide nanosheet-based composites, *Chem. Soc. Rev.*, 2015, 44(9), 2713–2731.
- 16 L. Liu, J. Zhang, J. Zhao and F. Liu, Mechanical properties of graphene oxides, *Nanoscale*, 2012, 4(19), 5910–5916.
- 17 X. Li and H. W. Zhu, Two-dimensional MoS₂: properties, preparation, and applications, *J. Mater.*, 2015, **1**(1), 33–44.
- 18 C. Y. Zhi, Y. Bando, C. C. Tang, H. Kuwahara and D. Golberg, Large-scal fabrication of boron nitride nanosheets and their utilization polymeric composites with improved thermal and meel an cal properties, *Adv. Mater.*, 2009, **21**(28), 2889–2893.
- 1º G Wang, X. G. Zhu, Y. Y. Sun, Y. Y. Li, T. Zhang, J. Wen, X. Chen, K. He, L. L. Wang, X. C. Ma, J. F. Jia, S. B. Zhang and Q. K. Xue, Topological insulator thin films of Bi₂Te₃ with controlled electronic structure, *Adv. Mater.*, 2011, 23(26), 2929–2932.
- 20 C. Tan, X. Cao, X. Wu, Q. He, J. Yang, X. Zhang, J. Chen, W. Zhao, S. Har, G. W. H. Nam, M. Sindoro and H. Zhang, Recent advances in ultrathin two-dimensional nanomaterials, Chen. Rev., 2017, 117(9), 6225–6331.
- 21 N. A. Limar, M. A. Dar, R. Gul and J. B. Baek, Graphene and probblenum disulfide hybrids: synthesis and applications, *Nater. Today*, 2015, **18**(5), 286–298.
- 22 M. Pumera and Z. Sofer, 2D monoelemental arsenene, antimonene, and bismuthene: beyond black phosphorus, *Adv. Mater.*, 2017, 29(21), 1–8.
- 23 J. H. Shen, Y. H. Zhu, H. Jiang and C. Z. Li, 2D nanosheets-based novel architectures: synthesis, assembly and applications, *Nano Today*, 2016, **11**(4), 483–592.
- 24 J. Zhu, E. Ha, G. L. Zhao, Y. Zhou, D. Huang, G. Z. Yue, L. S. Hu, N. Sun, Y. Wang, L. Y. S. Lee, C. Xu, K. Y. Wong, D. Astruc and P. X. Zhao, Recent advance in MXenes: a promising 2D materials for catalysis, sensor and chemical and adsorption, *Coord. Chem. Rev.*, 2017, 352, 306–327.
- 25 B. Radisavljevic, A. Radenovic, J. Brivio, V. Giacometti and A. Kis, Single-layer MoS₂ transistors, *Nat. Nanotechnol.*, 2011, **6**(3), 147–150.
- 26 A. Castellanos-Gomez, L. Vicarelli, E. Prada, J. Q. Island, K. Narasimha-Acharya, S. I. Blanter, D. J. Groenendijk, M. Buscema, G. A. Steele and J. Alvarez, Isolation and characterization of few-layer black phosphorus, 2D Mater., 2014, 1(2), 1–19.
- 27 S. Z. Karazhanov, P. Ravindran, A. Kjekshus, H. Fjellvag and B. G. Svensson, Electronic structure and optical properties

- of ZnX (X = O, S, Se, Te): a density functional study, *Phys. Rev. B: Condens. Matter Mater. Phys.*, 2007, 75(15), 155104.
- 28 J. Zhou, J. Huang, B. G. Sumpter, P. R. C. Kent, H. Terrones and S. C. Smith, Structures, energetics, and electronic properties of layered materials and nanotubes of cadmium chalcogenides, *J. Phys. Chem. C*, 2013, **117**(48), 25817–25825.
- 29 C. J. Tong, H. Zhang, Y. N. Zhang, H. Liu and L. M. Liu, New manifold two-dimensional single-layer structures of zinc-blende compounds, *J. Mater. Chem. A*, 2014, 2(42), 17971–17978.
- 30 J. Zhou, J. Huang, B. G. Sumpter, P. R. C. Kent, Y. Xie, H. Terrones and S. C. Smith, Theoretically predictions of freestanding honeycomb sheets of cadmium chalcogenides, *J. Phys. Chem. C*, 2014, 118(29), 16236–16245.
- 31 L. Li, P. Li, N. Lu, J. Dai and X. C. Zeng, Simulation evidence of hexagonal-to-tetragonal ZnSe structures transition: a monolayer material with a wide-range tunable direct bandgap, *Adv. Sci.*, 2015, 2(12), 1500290.
- 32 J. Zhou, B. G. Sumpter, B. R. C. Kent and J. Huang, A novel and functional single-layer sheet of ZnSe, *ACS Appl. Mater. Interfaces*, 2015, 7(3), 1458–1464.
- 33 J. Zhou, Y. Li, X. Wu and W. Qin, Modulating the electronic and optical properties of tetragonal ZnSe monolayer by chalcogen dopants, *ChemPhysChem*, 2016, 17(13), 1993–1998.
- 34 X.-D. Wen, R. Hoffmann and N. W. Ashcroft, Two-dimensional CdSe nanosheets and their interaction wit'. stabilizing ligands, *Adv. Mater.*, 2013, 25(2), 261–266.
- 35 S. Ithurria, M. D. Tessier, B. Mahler, R. P. S. M. obc B. Dubertret and A. L. Efros, Colloiddal nanoplatelets with two-dimensional electronic structure, *Nat. Mater.*, 2011, 10(12), 936–941.
- 36 S. Ithurria and B. Dubertret, Quasi 2D colleta CdSe platelets with thicknesses controlled at the tornic level, *J. Am. Chem. Soc.*, 2008, **130**(49), 16504–16503.
- 37 J. S. Son, X. D. Wen, J. Joo, J. Chae, S. I. Baek, K. Park, J. H. Kim, K. An, J. H. Yu, S. G. Kwon, S. H. Choi, Z. W. Wang, Y. W. Kim, Y. Kuk, R. Hoffmann and T. Hyeon, Large-sca'e soft colloidal template synthesis of 1.4 nm thicl¹ Cc Sc nanosheets, *Angew. Chem., Int. Ed.*, 2009, 48(37), 68: 1-8/4.
- 38 S. Ithurria, G. Bousquet and B. Dubertret, Continuous transition from 3D to 1D confinement observed during the formation of CdSe nanoplatelets, *J. An. Them. Soc.*, 2011, 133(9), 3070–3077.
- 39 Z. Li and X. Peng, Size/Shape-controlled synthesis of colloidal CdSe quantum disks: ligand and emperature effects, *J. Am. Chem. Soc.*, 2011, 133(17), 678–6586.
- 40 Y. Sun, Z. Sun, S. Gao, H. Cheng, Q. Liu, J. Piao, T. Yao, C. Wu, S. Hu, S. Wei and Y. Yie, Fabrication of flexible and freestanding zinc challogenide single layers, *Nat. Commun.*, 2012, 3, 1–7.
- 41 J. Zhou and X. Yu, A. w engineering of electronic and optical properties of enagonal monolayer zinc chalcogenides, *J. Alloys Comp.* 2017, **695**, 1392–1396.
- 42 J. Zhou and X. H. Wu, First-principle study on doping of tetragonal ZnSe monolayers, *Mater. Today Chem.*, 2017, 4, 40–44.

- 43 J. Zhou, H. Zhuang and H. Wang, Layered tetragonal zinc chalcogenides for energy related applications: from photocatalysts for water splitting to cathode materials for Li-Ion batteries, *Nanoscale*, 2017, 9(44), 17303–17311.
- 44 J. Zhou and X. Zhen, A theoretical perspective of the enhanced photocatalytic properties achieved by forming tetragonal ZnS/ZnSe hetero-bilayer, *Phys. Chem. Chem. Phys.*, 2018, **20**(15), 9950–9956.
- 45 G. Kresse and J. Hafner, Ab initio molecular dynamics for liquid-metal- amorphous-semiconductor transition in germanium, *Phys. Rev. B: Condens. Matter Mater. Phys.*, 1994, 49(20), 14251–14269.
- 46 G. Kresse and J. Hafner, Ab initio molecular dynamics for liquid metals, *Phys. Rev. B: Condens. Matter Mater. Phys.*, 1993, 47(1), 558–561.
- 47 K. Albe and J. Furthmüller, Efficient iterative schemes for ab initio total-energy calculations using a plane-wave basis set, *Phys. Rev. B: Condens. Matter Mater. Phys.*, 1996, 54(16), 11169–11186.
- 48 P. E. Blöchl, Projector augmented-wave method, *Phys. Rev. B: Condens Matter Mater. Phys.*, 1994, **50**(24), 17953–17979.
- 49 J. P. Per 'ev' K. Burke and M. Ernzerhof, Generalized gradient appr xir ation made simple, *Phys. Rev. Lett.*, 1996, 77(18), 3 65 3868.
- 50 H. J. Monkhorst and J. D. Pack, Special points for brillouinzone integrations, *Phys. P. J. Condens. Matter Mater. Phys.*, 1976, **13**(12), 5188–5102.
- 51 J. Heyd, G. E. Scuseria and M. Ernzerhof, Hybrid functionals based on a screener coulomb potential, *J. Chem. Phys.*, 2003, **118**(18) 9237-8215.
- 52 A. V. Krukou, O. A. Vydrov, A. F. Izmaylov and G. E. Scuseria, Influence of the exchange screening parameter on the perfortance of screened hybrid functionals, *J. Chem. Phys.*, 2005, 225, 224106.
- 53 S. Mcginley, M. Riedler and T. Möller, Evidence for surface econstruction on InAs nanocrystals, *Phys. Rev. B: Condens. Matter Mater. Phys.*, 2002, **65**, 2453308.
- 54 R. F. Bader, Atoms in molecules [M], Wiley Online Library, 1990.
- 55 G. Henkelman, A. Arnaldsson and H. Jonsson, A fast and robust algorithm for bader decomposition of charge density, *Comput. Mater. Sci.*, 2006, **36**(3), 354–360.
- 56 X. L. Ding, G. T. Yu, X. R. Huang and W. Chen, The donor/ acceptor edge-modification: an effective strategy to modulate the electronic and magnetic behaviors of zigzag silicon carbon nanoribbons, *Phys. Chem. Chem. Phys.*, 2013, 15(41), 18039–18047.
- 57 W. Chen, H. Zhang, X. L. Ding, G. T. Yu, D. Liu and X. R. Huang, Dihalogen edge-modification: an effective approach to realize the half-metallicity and metallicity in zigzag silicon carbon nanoribbons, *J. Mater. Chem. C*, 2014, 2(37), 7836–7850.
- 58 Q. Tang, Y. F. Li, Z. Zhou, Y. S. Chen and Z. F. Cheng, Tuning electronic and magnetic properties of wurtzite ZnO nanosheets by surface hydrogenation, *ACS Appl. Mater. Interfaces*, 2010, 2(8), 2442–2447.

Paper

59 (a) R. Tenne, M. Remškar, A. Enyashin and G. Seifert, Inorganic nanotubes and fullerene-like structures (IF), in *Carbon Nanotubes. Topics in applied physics*, ed. A. Jorio, G. Dresselhaus and M. S. Dresselhaus, Springer, Berlin, Heidelberg, 2007, vol. 111, pp. 631–671; (b) M. S. Dresselhaus and P. Avouris, Introduction to carbon materials research, in *Carbon Nanotubes. Topics in applied physics*, ed. M. S. Dresselhaus, G. Dresselhaus and P. Avouris, Springer, Berlin, Heidelberg, 2001, vol. 80, pp. 1–9.

- 60 I. R. Shein, A. N. Enyashin and A. L. Ivanovskii, Nanotubes of layered iron-based superconductors: simulations of atomic
- structure and electronic properties, *Comput. Mater. Sci.*, 2011, **50**(3), 824–827.
- 61 D. H. Hodges, A. Rajagopal, J. C. Ho and W. Yu, Stress and strain recovery for the in-plane deformation of an isotropic tapered strip-beam, *J. Mech. Mater. Struct.*, 2010, 5(6), 963–975.
- 62 J. Zhou, J. Lin, X. Huang, Y. Zhou, Y. Chen, J. Xia, H. Wang, Y. Xie, H. Yu, J. Lei, F. Liu, Q. Zeng, C.-H. Hsu, C. Yang, L. Liu, T. Yu, Z. Shen, H. Lin, B. I. Yakobson, K. Suenaga, G. Liu and Z. Liu, A library of atomically thin metal chalcogenides, *Nature*, 2018, 556(7701), 355–362.